Chapter 6

Enhancement of Single-Photon Sources with Metamaterials

M. Y. Shalaginov[1], S. Bogdanov[1], V. V. Vorobyov[2,4], A. S. Lagutchev[1], A. V. Kildishev[1], A. V. Akimov[2,3,4], A. Boltasseva[1], and V. M. Shalaev[1,*]

[1]*School of Electrical and Computer Engineering and Birck Nanotechnology Center, Purdue University, West Lafayette, IN 47907, USA,*
[2]*Moscow Institute of Physics and Technology, Dolgoprudny, Moscow Region,141700, Russia*
[3]*Russian Quantum Center, Skolkovo Innovation Center, Moscow Region, 143025, Russia*
[4]*Lebedev Physical Institute RAS, Moscow, 119991, Russia*

Scientists are looking for new, breakthrough solutions that can greatly advance computing and networking systems. These solutions will involve quantum properties of matter and light as promised by the ongoing experimental and theoretical work in the areas of quantum computation and communication. Quantum photonics is destined to play a central role in the development of such technologies due to the high transmission capacity and outstanding low-noise properties of photonic information channels.

Among the vital problems to be solved in this direction, are efficient generation and collection of single photons. One approach to tackle these problems is based on engineering emission properties of available single-photon sources using metamaterials. Metamaterials are artificially engineered structures with sub-wavelength features whose optical properties go beyond the limitations of conventional materials. As promising single-photon sources, we have chosen nitrogen-vacancy (NV) color centers in diamond, which are capable to operate stably in a single-photon regime at room temperature in a solid state environment.

In this chapter, we report both theoretical and experimental studies of the radiation from a nanodiamond single NV center placed near a hyperbolic metamaterial (HMM). In particular, we derive the reduction of excited-state lifetime and the enhancement of collected single-photon emission rate and compare them with the experimental observations. These results could be of great impact for future integrated quantum sources, especially owing to a CMOS-compatible approach to HMM synthesis.

*shalaev@purdue.edu

1. Introduction

The strongest driving force behind the study of quantum systems is to build quantum computing and networking technologies. These technologies would employ entirely different algorithms, unattainable for classical computers, that will reduce the complexity of a variety of computational problems. Among these problems are algorithmic searching,[1] number factorization,[2] and simulation of quantum systems.[3]

Low noise of photonic information channels and low cost of standard photonic device fabrication give photonics a central role in the development of quantum technologies. It seems probable that quantum information will be transmitted using quantum states of light and that at some degree information processing will be performed on these states.[5] The simplest and most fundamental quantum photonic states are single photons. The typical generation rates of available isolated single-photon sources are of the order of 100 kcounts per second. For fast communication and computation these rates have to be improved. In this chapter, we present our research towards the development of an efficient source of single photons.

1.1. *Available Single-photon Sources*

At present, several types of quantum systems capable of serving as truly deterministic single-photon sources have been investigated[7] (see Fig. 1), including trapped atoms[8] and ions,[9] single molecules,[10] quantum dots,[11] color centers,[12] atomic ensembles,[13] and mesoscopic quantum wells.[14] The solid state sources such as quantum dots and lattice defects are naturally interesting for future commercial quantum devices.

A nitrogen-vacancy (NV) color center in diamond, formed by a substitutional nitrogen atom and a vacancy at an adjacent lattice site, is a candidate of particular interest for the implementation of a solid state single-photon source.[15] It is resistant against photobleaching and operates at room temperature.[16] Its intrinsic quantum yield is close to unity[15] and it can be deterministically manipulated by a pick-and-place procedure.[17]

In addition, the diamond NV center gained significant attention thanks to its spin degree of freedom. Its electron spin state has coherence time in the range of milliseconds at room temperature,[21] far beyond that of, e.g., quantum dots made of III-V materials, and can be read out optically.[22] This unique spin-photon interface makes it possible to build reliable quantum-memory units[23] and perform high-fidelity single-shot projective quantum measurement.[24] Moreover, NV centers as solid-state structures are promising in sharing quantum entanglement among large number of qubits[25] and implementing scalable quantum information systems.[26] NV centers also could be used as sensors of electric[27] and magnetic[28] fields, temperature[29] and rotation[30] with high resolution and sensitivity.

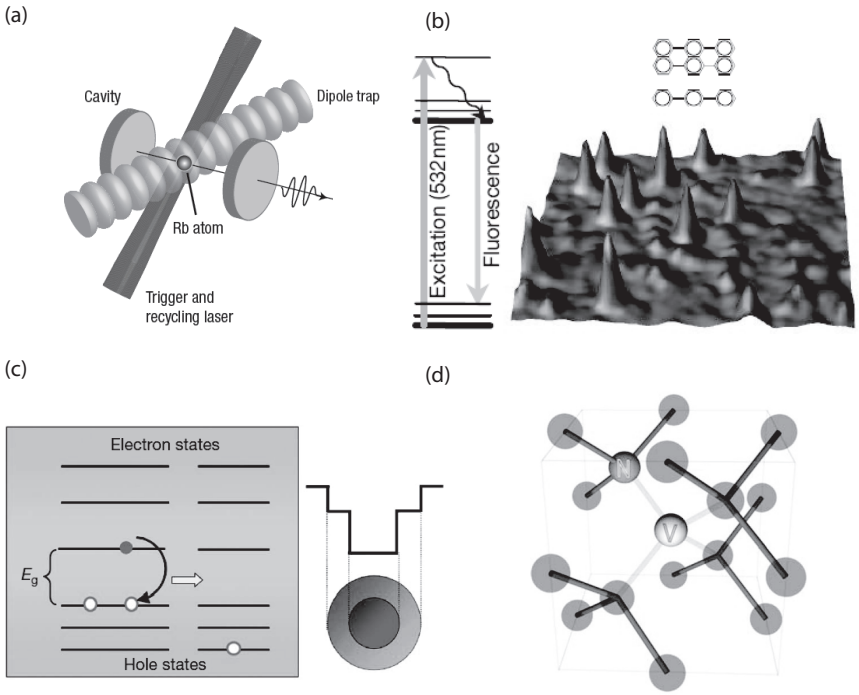

Fig. 1. Examples of available deterministic single-photon sources: (a) ^{85}Rb atom trapped in a high-finesse optical microcavity,[8] (b) single terrylene molecules in a p-terphenyl crystal,[18] (c) CdSe/ZnSe quantum dots,[19] (d) NV color centers in diamond.[20] Figures reproduced with permission: (a) Ref. [8] from Copyright 2007 NPG, (b) Ref. [18] from Copyright 2000 NPG, (c) Ref. [19] from Copyright 2009 NPG, (d) Ref. [20] from Copyright 2006 Wiley-VCH.

Strictly speaking, the NV center exists in two different charge states: the electrically neutral state NV^0 and the negatively charged state NV^-. In the rest of the chapter by "NV" we will refer to the NV^- state. The NV center can be identified thanks to the zero phonon line (ZPL) located at 637 nm. At room temperature the NV center emission spectrum exhibits phononic sideband that covers the range from 600 to 800 nm and the ZPL is largely obscured by this broadening. But even at liquid helium temperatures, only a few percent of the emission falls into the ZPL.[31] Therefore the NV center is intrinsically a broadband source.

1.2. *Methods of Spontaneous Emission Enhancement*

The applications using NV center as a single-photon generator and spin-photon interface could substantially benefit from enhanced emission rate and photon collection efficiency. Emission rate enhancement can be achieved by utilizing Purcell

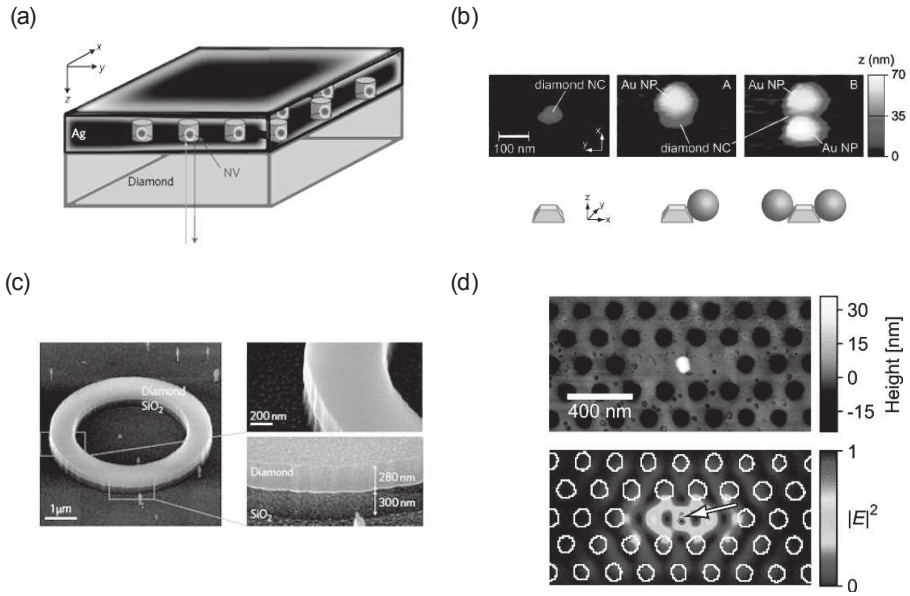

Fig. 2. Examples of resonance-based structures enhancing the emission from NV centers by coupling to (a) diamond silver apertures,[43] (b) gold nanoparticles,[44] (c) diamond microring resonators,[45] and (d) photonic crystal cavities.[34] Figures reproduced with permission: (a) Ref. [43] from Copyright 2011 NPG, (b) Ref. [44] from Copyright 2009 ACS, (c) Ref. [45] from Copyright 2011 NPG, (d) Ref. [34] from Copyright 2010 AIP.

effect.[32] So far, this has been accomplished by using resonant photonic structures (see Fig. 2), such as microspherical resonators,[33] photonic crystal microcavities,[34] and microring resonators,[45] which are all bandwidth limited. Tuning them to the exact frequency of a sharp transition is a considerable technological challenge. The Purcell effect in these systems strongly depends on the position of the emitter with respect to the mode power density profile. In addition, resonant structures limit the emitter response time. In the case of NV center at room temperature the resonant techniques would be unapplicable anyway in view of its broad emission spectrum (600-800 nm) and the development of new broadband enhancement techniques is being sought.

Coupling NV centers to hyperbolic metamaterials (HMM)[46–49] allows for the spontaneous emission to be enhanced over a broad spectral range. This enhancement is a result of a broadband singularity in the photonic local density of states (LDOS) within the HMM.[50–54]

The photonic LDOS, similar to its electronic counterpart, can be quantified as the volume in k-space between iso-frequency surfaces. For extraordinary waves in a uniaxial anisotropic medium with dielectric tensor $\overleftrightarrow{\varepsilon} = diag\left(\varepsilon_{\parallel}, \varepsilon_{\parallel}, \varepsilon_{\perp}\right)$, the iso-frequency surfaces are defined by the following equation:

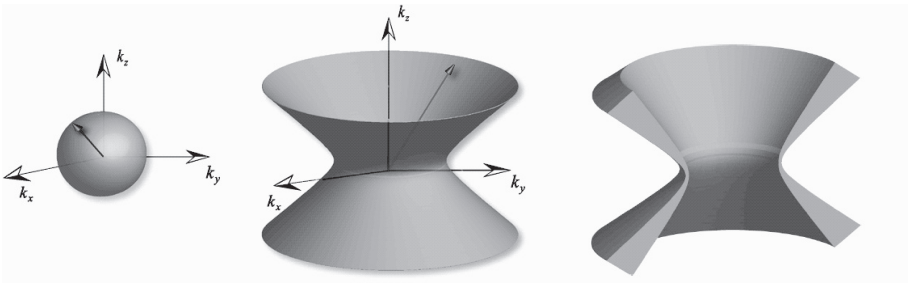

Fig. 3. Iso-frequency surfaces in the case of an isotropic dielectric (spheroid) and an extremely anisotropic medium with hyperbolic dispersion (hyperboloid).[53] Figure reproduced with permission from Copyright 2010 SSBM.

$$\omega^2/c^2 = k_{\parallel}^2/\varepsilon_{\perp} + k_{\perp}^2/\varepsilon_{\parallel}, \tag{1}$$

where subscripts "$\perp$"and "$\parallel$" indicate the directions perpendicular and parallel to the plane of anisotropy, respectively. In the case of dielectric materials with $\varepsilon_{\perp}, \varepsilon_{\parallel} > 0$, LDOS is equivalent to the volume of an infinitesimally thin ellipsoidal shell in k-space (see Fig. 3, left). However, in a medium with hyperbolic dispersion, $\varepsilon_{\perp}$and $\varepsilon_{\parallel}$ are of opposite signs which produces a hyperboloidal shell (see Fig. 3, middle and right) whose volume is infinitely large (i.e. broadband singularity in LDOS appears). As a result, such a medium allows the propagation of high-k modes with arbitrarily large wavevectors.

The HMM is practically realized as a lamellar structure consisting of alternating subwavelength-thick layers of metal and dielectric,[51,55] or as an array of nanowires embedded into a dielectric host matrix.[50,56] Between the two approaches to implement HMMs, planar HMMs are important from a technological point of view, as they can be fabricated using existing planar processing techniques. In these practical implementations, the maximum value of the wavevector is restricted by the size of the metamaterial unit cell and hence the singularity disappears. However, with nanometer-size layers even the available k-space yields a very high photonic LDOS, providing extra radiative channels for the coupled emitter. These channels are high-k metamaterial modes which result from hybridization of surface plasmon polariton modes at the interfaces of the layers constituting the HMM.[57]

In this chapter, the radiation from a nanodiamond single NV center placed near a hyperbolic metamaterial is studied both theoretically and experimentally.[58] The chapter is organized in the following way. First, we discuss sample fabrication and characterization as well as the experimental setup for NV center optical lifetime and collected power measurement. Next, we provide theoretical estimates of these quantities as a function of experimental parameters such as separation distance between an emitter and HMM surface and presence of scattering particles in the vicinity of the emitter. Then, we proceed with the discussion of the experimentally obtained results.

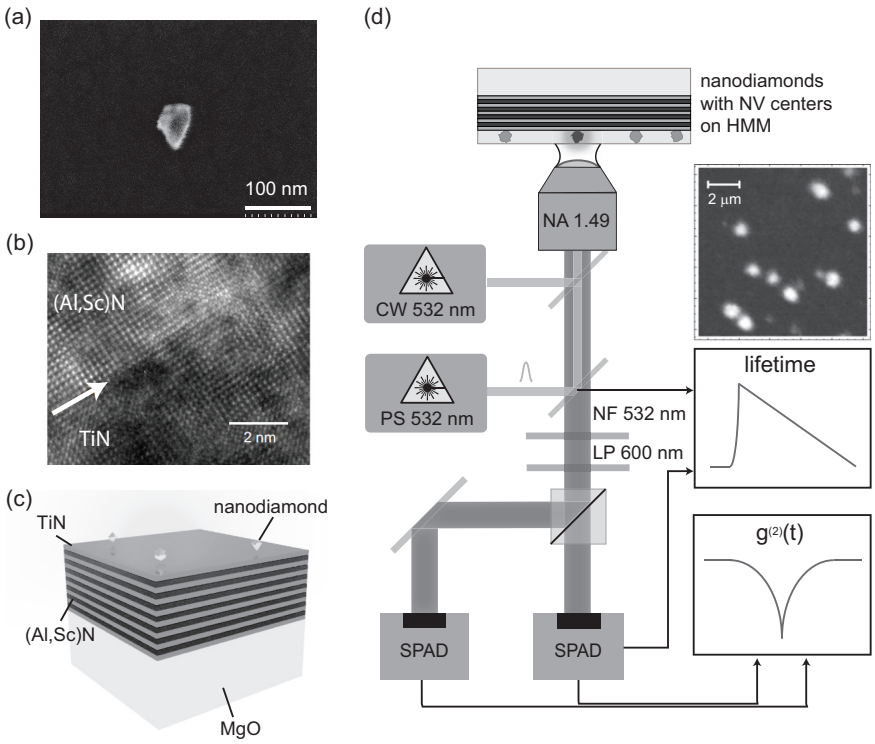

Fig. 4. (a) SEM scan of a ND on top of the HMM sample.[58] (b) HRTEM image showing the interface of TiN and (Al,Sc)N matching lattices in the superlattice.[61] (c) Sample structure and (d) schematic of the fluorescence analysis setup.[58] Figures reproduced with permission: (a), (c), (d) Ref. [58] from Copyright 2014 Wiley-VCH and (b) Ref. [61] from Copyright 2014 USNAS.

2. Experiment

Here we outline the details of the experiment aimed at studying radiation from single NV center nanodiamonds coupled to an epitaxially grown HMM superlattice composed of titanium nitride (TiN) and aluminum scandium nitride ($Al_xSc_{1-x}N$).[61]

2.1. *Nanodiamond Samples*

An aqueous suspension of nanodiamonds (NDs) with nominal size of 50 nm, 0.5% w/v was obtained from Microdiamant AG. The size of NDs was chosen according to a previous study, which showed that NDs with the size of 50-70 nm have the highest probability to host a single NV center.[66] However, the suspension also contained NDs smaller than the nominal size. The smallest NDs were eliminated and the suspension was cleaned by a multistep procedure. First, the suspension was centrifuged at 5000 rpm for 5 minutes. The supernatant (80% volume fraction) was then replaced with distilled water and the suspension was shaken until homogeneity.

The above procedure was repeated 5 times. Subsequently, a 20 μl droplet of the processed suspension was spin-coated onto a superlattice sample at 2000 rpm for 2 minutes. As a result, NDs with average size close to 50 nm were observed at the HMM surface as shown by the SEM scan in Fig. 4(a). Finally, the sample was covered with a 60-nm-thick layer of polyvinyl alcohol (PVA, 1.5% w/v) to guarantee the immobility of the NDs. In addition, the PVA layer separated the NDs from the immersion oil which was employed in the microscope setup for efficient collection of emitted light by an objective lens with high numerical aperture.

The reference sample consisted of NDs deposited by the same method onto a standard 150-μm-thick glass coverslip (VWR VistaVision^{TM} Cover Glasses, No. 1). Since the dielectric permittivities of these glass substrates (2.34) are close to those of the immersion oil (2.31) and the PVA layer (2.25) [78], the NDs in reference samples were considered as being effectively immersed into an infinite homogeneous medium with a permittivity of 2.25.

2.2. *Fabrication and Characterization of HMM*

TiN is a new plasmonic material known for its CMOS compatibility, mechanical strength, and thermal stability at high temperatures (melting point > 2700°C).[62,63] This material can be epitaxially deposited on a variety of different substrates, such as magnesium oxide, silicon, aluminum scandium nitride, sapphire, down to thickness of a few nanometers. Conventional plasmonic materials (e.g. gold or silver) cannot form continuous layers of such thicknesses. This property is of fundamental importance for increasing LDOS, since LDOS for multilayer HMM is inversely proportional to the cube of the layer thickness.[64,65]

Our HMM consisted of a TiN/$Al_{0.7}Sc_{0.3}N$ superlattice epitaxially grown on a [001]-oriented magnesium oxide (MgO) 0.5-mm-thick substrate using reactive DC magnetron sputterer (PVD Products) with a base pressure of 10^{-7} torr at 750°C. The superlattice was formed by a stack of 10 pairs of layers each consisting of 8.5-nm-thick film of TiN and 6.3-nm-thick film of $Al_{0.7}Sc_{0.3}N$ similar to the structure reported in Ref. [61]. Fig. 4(b) shows the cross-sectional high-resolution TEM image of the superlattice with matching latices of TiN and (Al,Sc)N.[61] The NDs were spun on top of the HMM as shown in Fig. 4(c). Since the TiN and (Al,Sc)N layer thicknesses were much smaller than the wavelength of light, the HMM can be approximated as a uniaxial anisotropic effective medium with dielectric permittivities $\varepsilon_{\parallel}$ and $\varepsilon_{\perp}$.[68] The latter were measured using a spectroscopic ellipsometer (J. A. Woollam Co.; W-VASE).[59] The dielectric permittivities of the constituent materials (TiN and $Al_{0.7}Sc_{0.3}N$) as well as substrate (MgO) were retrieved from the values of Ψ and Δ measured in the wavelength range 300 – 2000 nm at angles of incidence 50° and 70°. The Drude-Lorentz model used for data fit is the following:

$$\varepsilon(\hbar\omega) = \varepsilon_1 + i\varepsilon_2 = \varepsilon_\infty + \sum_k \frac{A_k}{E_k^2 - (\hbar\omega)^2 - iB_k\hbar\omega}, \quad (2)$$

Table 1. Experiment-fitted parameters of the Drude-Lorentz model for (Al,Sc)N and TiN films.[58] Table reproduced with permission from Copyright 2014 Wiley-VCH.

	TiN	(Al,Sc)N
ε_∞	4	4
A_1 (eV)^2	52.536	0
B_1(eV)	0.29197	0
A_2(eV)^2	130.93	11.162
B_2(eV)	4.9807	0.63261
E_2(eV)	5.9784	3.6857

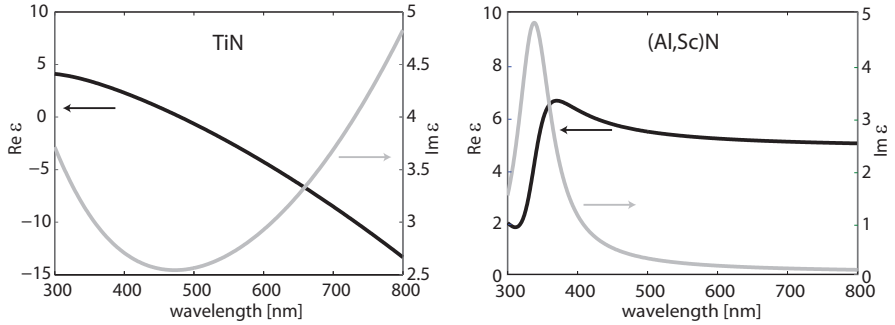

Fig. 5. The dielectric functions of TiN and (Al,Sc)N: real and imaginary parts are shown with black and light gray lines, respectively.[58] Figure reproduced with permission from Copyright 2014 Wiley-VCH.

where $\hbar$ is the reduced Plank's constant, A_k is the amplitude, E_k is the center energy and B_k is the broadening of each oscillator.[69] The experiment-fitted parameters are presented in the Table 1. The corresponding dependences of the TiN and (Al,Sc)N dielectric functions (Re ε, Im ε) versus wavelength are plotted in Fig. 5.

The TiN-based metamaterial exhibited hyperbolic dispersion in the wavelength range of the NV center emission (600-800 nm, Fig. 6, highlighted area): with $\varepsilon_\perp = 16.4+i21.1$ and $\varepsilon_\parallel = -2.3+i2.1$ at emission peak wavelength (685 nm). Thus, for the electric field parallel to the interface, the metamaterial at this wavelength behaved as a metal. However, at the excitation wavelength of 532 nm (Fig. 6, vertical dashed gray line) the TiN/(Al,Sc)N metamaterial behaved as a lossy dielectric with $\varepsilon_{||} = 1.27 + i1.6$, allowing for transmission of the tangential component of the pump electric field. This facilitated efficient delivery of the excitation field to the NV center. The transmittance, reflectance and absorbance spectra of the HMM are shown in Fig. 7.

2.3. *Experimental Setup*

The increase in the spontaneous emission rate, the reduction of the excited state lifetime, and the second-order correlation function of the emission were measured using

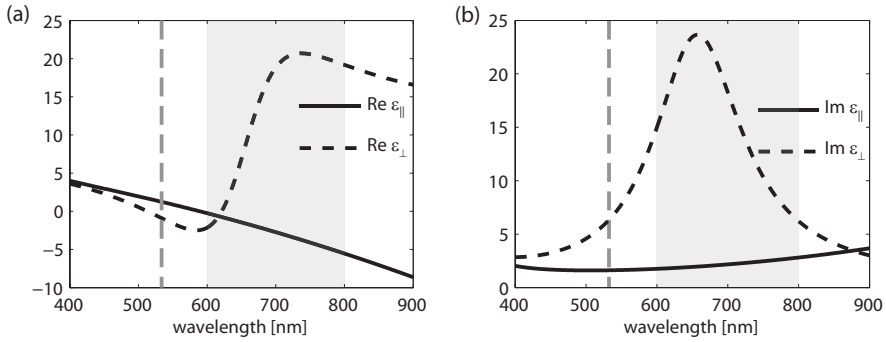

Fig. 6. (a) Real and (b) imaginary parts of the dielectric functions of the uniaxial effective medium that approximates the fabricated HMM.[58] The permittivities were obtained by spectroscopic ellipsometry. Within the range of the NV center emission (600-800 nm-highlighted), the metamaterial showed hyperbolic dispersion (Re[$\varepsilon_\perp$] >0, Re[$\varepsilon_\parallel$] <0). At the excitation wavelength (532 nm, vertical dashed gray line) the metamaterial behaved as a lossy dielectric. Figures reproduced with permission from Copyright 2014 Wiley-VCH.

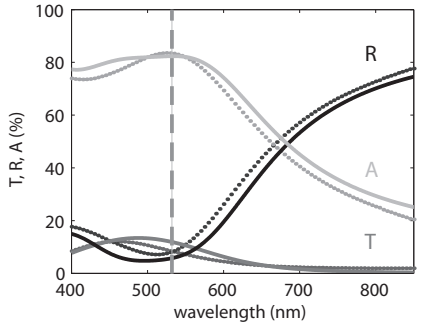

Fig. 7. Transmittance (T), reflectance (R), and absorbance (A) of the TiN HMM calculated using direct T-matrix method (solid lines)[84] and measured by spectrophotometry (dotted lines); angle of incidence for $T - 0°$, for $R - 8°$; $A = 1 - T - R$.[58] Figure reproduced with permission from Copyright 2014 Wiley-VCH.

a home-made confocal microscope, which is schematically represented in Fig. 4(d). The fluorescent radiation from an NV center was collected with a wide aperture (NA = 1.49) oil immersion objective (Nikon; CFI Apo TIRF 100X Oil) and separated from the pump with a series of optical filters. A single-photon avalanche photodiode, SPAD (PerkinElmer; SPCM-AQRH-14-FC) was used as a detector. Statistical measurement of the time delay between the excitation pulse and the first detected fluorescence photon, known as time-correlated single-photon counting (TCSPC),[70] has been employed. The lifetime was obtained from the exponential fit of the fluorescence decay histogram. The excitation of NV center for fluorescence lifetime measurements was performed by 532-nm picosecond pulsed laser

(PicoQuant; LDH-P-FA-530XL). The setup was converted as necessary to a Hanbury Brown-Twiss interferometer[71] to measure the second-order correlation function $g^{(2)}(t)$ by addition of a 50/50 beamsplitter and a second avalanche photodiode with a coaxial cable 80-ns-delay line. In this configuration, the NV centers were excited by a 532 nm continuous-wave laser (Coherent; Compass 315M-100). The measurement of $g^{(2)}(t)$ allows to identify NDs with single NV centers. $g^{(2)}(t)$ was obtained by measuring the background corrected coincidence count rate, normalized by the total counts on each detector, time-bin width and data collection time.[72] For a single-photon emitter the $g^{(2)}(t)$ curve is expected to exhibit a dip around $t = 0$ due to impossibility of simultaneous photon arrival at both detectors. The measured dip was fitted with the expression $\exp(-[\Gamma + R]|t|)$, where Γ and R are the total decay rate and pump rate, respectively. The signal from SPAD was processed by an electronic correlation module (PicoHarp 300, PicoQuant).

3. Theory

In this section, we calculate the spontaneous emission rate (represented by the Purcell factor F_P) and the normalized emission power f_{rad} collected in the far-field by an objective located above the HMM surface. Rigorous account of the spontaneous emission process can only be done in the frame of quantum electrodynamics. Since our quantum emitter is weakly coupled to the metamaterial environment, a calculation of the above parameters based on principles of classical electrodynamics is expected to be in reasonable agreement with the experiment.[73] In order to model our system, we considered the problem of dipole radiation near a planar layered medium, which is described in more detail in Refs. [74–76].

3.1. *Semi-analytical Calculations of the Purcell Factor and Normalized Collected Emission Power*

A single emitter was modeled as an oscillating electric dipole with dipole moment $\mathbf{p}$ and angular frequency ω. The energy dissipation rate in an inhomogeneous environment is given by[76]

$$P = \frac{\omega}{2} Im\left[p^* \cdot (E_0(r_0) + E_s(r_0))\right], \tag{3}$$

where $E_0(r_0)$ and $E_s(r_0)$ are the primary dipole field and scattered field at the dipole position (r_0), respectively. These electric fields were calculated using the dyadic Green's function formalism.[76] We analyzed the contribution of each spatial frequency mode (k-mode) using angular spectrum representation of the Green's functions.

The inset in Fig. 8(a) depicts an oscillating dipole situated at height h above the HMM uppermost layer ($Al_{0.7}Sc_{0.3}N$), the upper half-space (superstrate) filled with homogeneous medium with $\varepsilon_{sup} = 2.25$, planar multilayer $TiN/Al_{0.7}Sc_{0.3}N$

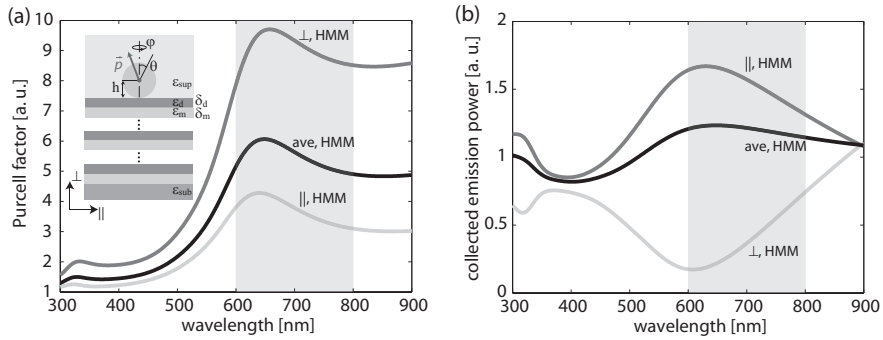

Fig. 8. Calculated estimates of Purcell factor (a) and collected emission power (b) for a dipole located in homogeneous medium with $\varepsilon_{sup} = 2.25$ at the distance of 25 nm above the HMM surface.[58] Dark gray, light gray, and black curves correspond to the dipole orientations perpendicular ($\perp$), parallel ($\|$) to the HMM interface, and averaged (ave), respectively. Highlighted area indicates the emission spectral range of NV center at room temperature. Collection angle is 79.6°, which corresponds to NA 1.49. Layout of the modeled structure is shown in the inset. Figures reproduced with permission from Copyright 2014 Wiley-VCH.

superlattice ($\varepsilon_m/\varepsilon_d$) and the lower half-space (substrate) made of MgO (ε_{sub}). For this simulation we considered the HMM, used in our experiments, consisting of 10 pairs of 8.5-nm-thick TiN and 6.3-nm-thick (Al,Sc)N on MgO substrate. The Purcell factors F_P for in-plane ($\|$) and perpendicular ($\perp$) oriented single-dipole emitters placed at a distance h above a multilayer planar structure were calculated using the following formulae[76]

$$F_P^{\perp} = 1 + \frac{3}{2}\frac{1}{\varepsilon_{\rm sup}^{3/2}}\int_0^{\infty} Re\left\{\frac{s^3}{s_{\perp,\rm sup}(s)}\tilde{r}^p(s)e^{2ik_0 s_{\perp,\rm sup}(s)h}\right\}ds, \tag{4}$$

$$F_P^{\|} = 1 + \frac{3}{4}\frac{1}{\varepsilon_{\rm sup}^{1/2}}\int_0^{\infty} Re\left\{\frac{s}{s_{\perp,\rm sup}(s)}\left[\tilde{r}^s(s) - \frac{s^2_{\perp,\rm sup}(s)}{\varepsilon_{\rm sup}}\tilde{r}^p(s)\right]e^{2ik_0 s_{\perp,\rm sup}(s)h}\right\}ds. \tag{5}$$

The value of F_P for the averaged (ave) dipole orientation is given by

$$F_P^{iso} = \frac{2}{3}F_P^{\|} + \frac{1}{3}F_P^{\perp}. \tag{6}$$

The normalized collected emission powers f_{rad} for the same dipole orientations are

$$f_{rad}^{\perp} = \frac{3}{4}\int_0^{\theta_{\max}} \sin^3\theta \left| e^{-i\varepsilon_{\sup}^{1/2}k_0 h\cos\theta} + \tilde{r}^p(\theta) e^{i\varepsilon_{\sup}^{1/2}k_0 h\cos\theta}\right|^2 d\theta, \tag{7}$$

$$f_{rad}^{\parallel} = \frac{3}{8}\int_0^{\theta_{\max}} \left(\cos^2\theta \left| e^{-i\varepsilon_{\sup}^{1/2}k_0 h\cos\theta} - \tilde{r}^p(\theta) e^{i\varepsilon_{\sup}^{1/2}k_0 h\cos\theta}\right|^2 + \left| e^{-i\varepsilon_{\sup}^{1/2}k_0 h\cos\theta} + \tilde{r}^s(\theta) e^{i\varepsilon_{\sup}^{1/2}k_0 h\cos\theta}\right|^2\right) \sin\theta d\theta, \tag{8}$$

$$f_{rad}^{iso} = \frac{2}{3} f_{rad}^{\parallel} + \frac{1}{3} f_{rad}^{\perp}. \tag{9}$$

In equations (4) - (9), $s = k_{\parallel}/k_0$, $s_{\perp,\sup}(s) = k_{\perp,\sup}(s)/k_0 = \left(\varepsilon_{\sup} - s^2\right)^{1/2}$, $k_0 = \omega/c$, θ is a polar angle measured from the $\perp$ direction, the collection angle $\theta_{max} = 79.6°$. $k_{\parallel}$ is the in-plane component of the k-vector varying from 0 to infinity. The generalized superlattice′s Fresnel reflection coefficients for p- and s-polarized light $\tilde{r}^p$ and $\tilde{r}^s$ were calculated utilizing the recursive imbedding method (see Appendix), which is more precise and efficient than the direct transfer matrix approach.[77] The integrals were numerically evaluated by using an adaptive Gauss–Kronrod quadrature method.[78] In the formulae, we assumed that intrinsic quantum yield of NV centers is close to unity.[79] F_P and f_{rad} were normalized by the total radiation power and the power emitted into the collection angle, respectively. Both powers corresponded to the case of the emitter immersed into homogeneous medium with dielectric permittivity ε_{sup}, which models well the reference sample in the experiment.

In Fig. 8 we represent the calculated F_P and f_{rad} for in-plane (light gray), perpendicular (dark gray) and averaged (black) dipole orientations as a function of emission wavelength. The values of F_P and f_{rad} for the averaged orientation are defined as statistical averages of F_P and f_{rad} over all possible orientations. Assuming that the NV center is located at the crystal center, the expected Purcell factor for the NDs with a mean diameter of 50 nm should be on average around 4.5. The detected count rates corresponding to the normalized collected emission power for the same type of NDs were anticipated to increase on average by about 20%. The estimates for F_P and f_{rad} are modest in our experimental configuration. In the next two subsections we will show that the experimental conditions can be optimized to obtain higher values of both quantities.

3.2. *Dependence of F_P and f_{rad} on the Distance between an Emitter and HMM Surface*

The Purcell factor F_P increases as the separation distance h between the emitter and the surface is reduced. This is a common feature for dipoles located near metallic surfaces[4] and is expected to be observed as well in the case of an NV center on

HMM. In our case, the smallest separation distance is dictated by the ND size. The Purcell factor dependence on h is explained by the fact that at short distances h the evanescent fields created by the emitter are better coupled to the metamaterial modes.[85]

We have calculated the Purcell factor as a function of h for different orientations of a dipole located in the homogeneous medium above the HMM structure previously described (see Fig. 9(a)). At the distance of 25 nm, corresponding to the size of our NDs, the Purcell enhancement is on the order of 10, as shown in Fig. 8. However, at distances h of a few nanometers the Purcell factor reaches two orders of magnitude.

In Fig. 9(b) we represent the dependence of f_{rad} on h. The averaged f_{rad} improvement (black curve) from different dipole orientations drops down from 23% to 0% as h decreases from 25 nm to zero. However, for the in-plane and out-of-plane dipole orientations considered separately, the trends are opposite, which can be understood as an interference effect. The collective behavior of free electrons in a metal can be represented as an oscillation of an image dipole. The interference happens between the real and image dipole sources whose relative phase and amplitudes are dictated by the complex generalized reflection coefficients $\tilde{r}^p$ and $\tilde{r}^s$ calculated in Appendix.[4]

Thus, bringing the dipole closer to the metamaterial allows for better energy coupling to metamaterial modes. However, this increase in the Purcell factor does not translate into higher collected emission power, which encourages to look for techniques of metamaterial mode outcoupling.

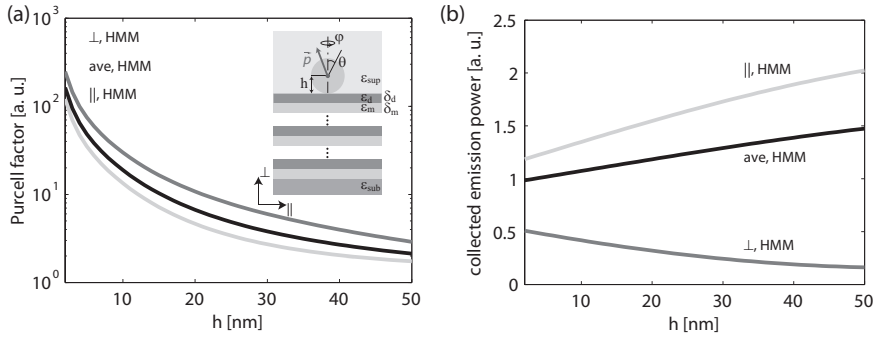

Fig. 9. Dependencies of the Purcell factor F_P (a) and the collected emission power f_{rad} (b) on a dipole position h above the HMM surface.[58] Dark gray, light gray, and black curves correspond to the dipole orientations perpendicular ($\perp$), parallel ($\|$) to the HMM interface and averaged (ave), respectively. Figures reproduced with permission from Copyright 2014 Wiley-VCH.

3.3. *Influence of Neighboring NDs and Structural Surface Defects of HMM on Collected Emission Power*

The coupled plasmonic modes are collective oscillations of electromagnetic field and electron plasma in the metallic layers of the HMM. One can expect the coupled plasmonic modes (corresponding to $k_{\|} > \sqrt{\epsilon_{sup}}k_0$) to be efficiently outcoupled to low-k superstrate modes via small size structural irregularities. Examples of such irregularities (adacent nanodiamonds and superlattice defects) are demonstrated in Fig. 10(a). To qualitatively estimate the influence of these scattering objects, we have performed finite-element method (FEM) analysis using a commercial numerical simulation tool (COMSOL Multiphysics). Beforehand, we have checked the consistency of the FEM with the semi-analytical method in the case of planar HMM without any scatterers and obtained a reasonable agreement between the two methods (Fig. 11). Then, we have simulated the power emitted by the dipole

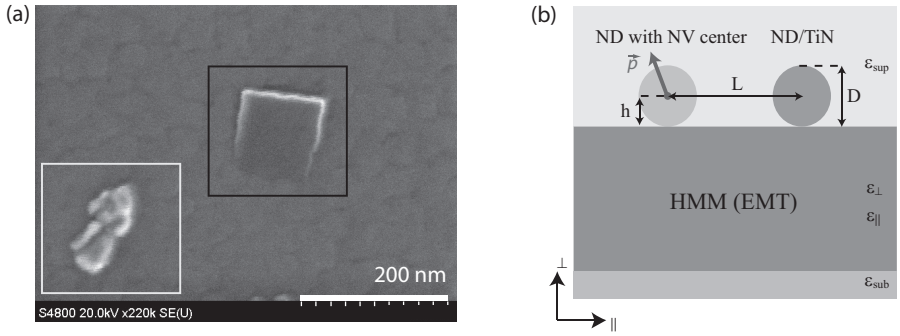

Fig. 10. (a) SEM scan showing a superlattice defect (inside black frame) and agglomerated NDs (inside white frame). (b) Schematic of the simulated structure.[58] Figures reproduced with permission from Copyright 2014 Wiley-VCH.

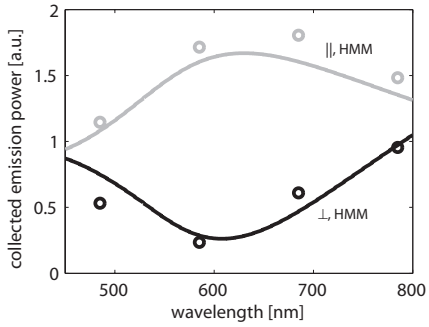

Fig. 11. Agreement between semi-analytical (solid lines) and FEM calculations (circles). The calculations are performed for the HMM without any scatterers. Black and light gray curves correspond to the dipole orientations perpendicular (⊥) and parallel (||) to the HMM interface, respectively.[58] Figure reproduced with permission from Copyright 2014 Wiley-VCH.

Table 2. Influence of NDs lacking NV centers and structural surface defects (TiN particles) on normalized collected emission power f_{rad}. Demonstrated values are the enhancement factors of f_{rad}.[58] Table reproduced with permission from Copyright 2014 Wiley-VCH.

	on HMM	on HMM with ND			on HMM with TiN particle		
		10 nm	69 nm	343 nm	10 nm	69 nm	343 nm
in-plane (∥)	1.8	2.3	1.8	1.8	3.9	1.9	1.8
perpendicular (⊥)	0.6	0.6	0.6	0.6	0.2	0.4	0.6
isotropic (iso)	1.5	1.9	1.5	1.5	3.0	1.5	1.5

source on top of HMM in the presence of a spherical scatterer. The schematic of the simulated structure is shown in Fig. 10(b). The HMM was considered as an effective anisotropic medium, whereas scatterers are modelled as either diamond or TiN spheres of 50 nm in diameter. The emitter was emulated as an electric point dipole embedded into a 50-nm-diameter diamond sphere. The superstrate and substrate are respectively the immersion oil and MgO. Three values of emitter-scatterer distance of 10, 69 and 343 nm have been considered. The emission wavelength was fixed to 685 nm.

Results of the FEM simulations, the enhancement factors of f_{rad} values, are summarized in Table 2. The noticeable influence is observed at small separation distances. For the averaged dipole orientation, an adjacent (at a distance of 10 nm) ND or TiN scatterer can increase f_{rad} by 30% or 200%, respectively. For an in-plane oriented emitter, the increase in emitted power from a nearby surface defect is up to 220%, giving an overall emission enhancement factor of 4 compared to the emitter on coverslip.

4. Results and Discussions

The NDs with single NV centers were selected by measuring the second-order correlation function $g^{(2)}(t)$ of the radiation from the detected fluorescence spots. Only NV centers with $g^{(2)}(0) < 0.5$ were considered for further experiments. This is a commonly accepted criterion for antibunched emission that is characteristic of a single photon source.[86] Typical photon antibunching effect is shown for a single NV center on glass coverslip and on HMM in Fig. 12.

We retrieved the total NV centers lifetimes from the exponential fitting of the fluorescence decays such as the ones shown in Fig. 13(a). The average values measured were 17.1 ns and 4.3 ns on glass and HMM, respectively (see Fig. 13(b)). Hence, the NV centers on HMM exhibit an average decrease in lifetime by a factor of 4, which is consistent with the above Purcell effect calculations. The shortest recorded lifetime for a single NV center on top of HMM is 1.5 ns, which corresponds to a Purcell factor of 11.4. The spreads in the lifetime statistics are likely due to the variation in NV center distance from the HMM surface and its dipole orientation.

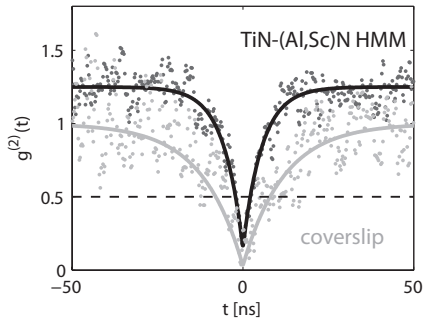

Fig. 12. Second-order correlation function $g^{(2)}(t)$ of the emission from a representative ND with single NV center on top of coverslip and HMM.[58] Figure reproduced with permission from Copyright 2014 Wiley-VCH.

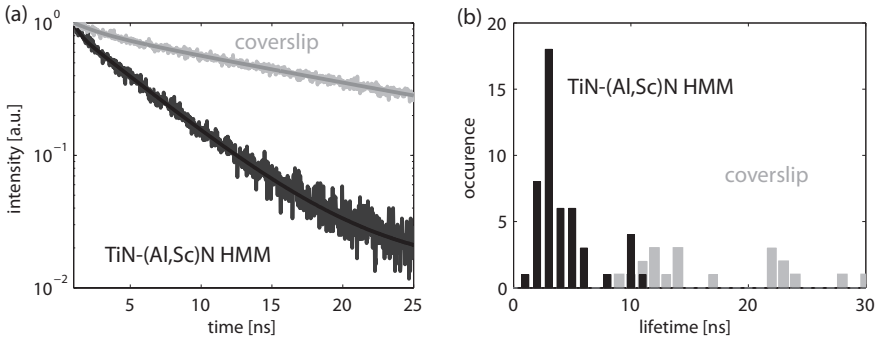

Fig. 13. (a) Representative normalized fluorescence decays and (b) histograms of lifetimes for the NV centers located on glass coverslip (reference sample) and on HMM.[58] The average and the lowest recorded lifetimes on HMM are 4 and 11.4 times shorter, respectively, than the average lifetime recorded on coverslip. Figures reproduced with permission from Copyright 2014 Wiley-VCH.

The single-photon emission rate dependences versus the excitation power are shown in Fig. 14(a), for the brightest NV centers on both the HMM and the glass coverslip. The data have been corrected for the background emission measured at a ND-free location. The emission count rate saturates around 1 mW of pump power. By fitting the experimentally measured saturation curves using the expression $I(P) = I_0/\left(1 + P_{sat}/P\right)$[87] we obtain the saturated single-photon count rates for each individual NV center. The histograms of these saturated single-photon count rates are shown in Fig. 14(b) for the NV centers both on glass and on HMM. The histogram corresponding to the HMM presents multiple groups. The NV centers in the group around 200 kcounts/s present an average enhancement against the coverslip of 1.8±1.1. This enhancement is consistent with the predicted value of 1.2, within the error margin. This large error is due to the enhancement value being the ratio of two measured parameters both having significant uncertainties

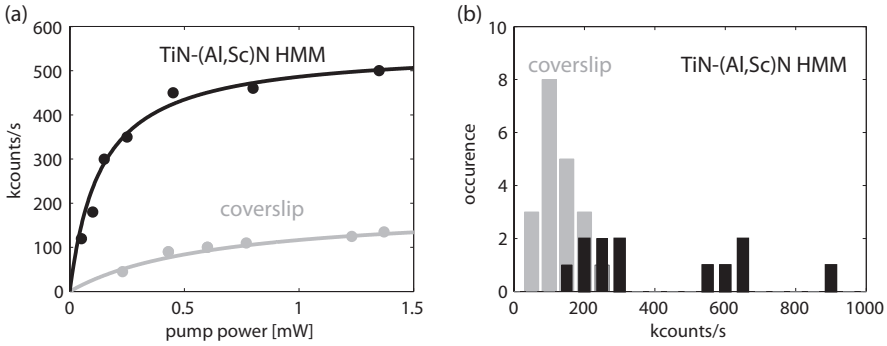

Fig. 14. Collected single-photon count rates (corrected for background emission) from NV centers in 50 nm NDs.[58] (a) Typical saturation curves and (b) histograms of count rates for NDs on glass coverslip (light grey) and HMM (black). The average count rate enhancements for the first and second group are 1.8 and 4.7, respectively. Figures reproduced with permission from Copyright 2014 Wiley-VCH.

due to random dipole orientation. The effect of h on collected power uncertainty is negligible as it follows from Fig. 9. The NV centers in the next group in the HMM histogram present an average count rate enhancement of 4.7±2.2, which is beyond the theory prediction. Finally there is one diamond showing even higher count rate enhancement. Excessive emission rates from certain NDs potentially could arise from the influence of either neighboring superlattice defects or adjacent "dark" NDs lacking NV centers.

The results of section 3.3 suggest that a substantial portion of the photons emitted by the dipole in the vicinity of HMM surface gets converted into high-k modes.[64] Once excited, these modes propagate through the HMM never leaving its bulk where they are eventually absorbed and do not provide any contribution to the collected photon flux. However, the presence of surface scatterers may result in outcoupling of these modes into the far field and therefore provide additional contribution to the emitted signal. We have shown above that taking into account energy outcoupling from defects surrounding the NV center can account for a further twofold increase in collected power and constitute a plausible cause for the observed count rate enhancement.

5. Summary

We have experimentally demonstrated an improvement in the emission rate of single NV centers in NDs placed on top of an epitaxial, TiN/(Al,Sc)N hyperbolic metamaterial compared to an isotropic environment with a uniform permittivity. The observed average lifetime decreased from 17 ns to 4.3 ns, corresponding to a Purcell factor of 4. This result is in good agreement with the theoretical prediction for an emitter located 25 nm away from the HMM surface. At the same time the collected emission power for NV centers near the hyperbolic metamaterial was increased by a

factor of 1.8 on average compared to NV centers on coverslip, although an enhancement of 4.7 was detected for several NV centers. The enhancement effect does not depend on in-plane location and does not require deterministic ND placement. At the same time, the emission rate of the ND-based single-photon source could be further enhanced by placing it closer to the surface of a TiN/(Al,Sc)N hyperbolic metamaterial. Most of the dipole emission is coupled to the hyperbolic metamaterial modes that are not directly detected in the far field. However, a significant portion of this power can be recovered in the far field by the presence of an adjacent growth defect or specifically engineered nanostructure. The results of this research can be used to build a highly efficient room temperature CMOS-compatible single-photon source.

Acknowledgments

The authors would like to thank R. Chandrasekar, J. Liu, M. Ferrera, J. Irudayaraj, V. V. Klimov, and A. N. Smolyaninov for their help with chapter preparation. This work was partially supported by the AFOSR-MURI grant (FA9550-10-1-0264) and NSF-MRSEC grant (DMR-1120923).

References

1. L. K. Grover, A fast quantum mechanical algorithm for database search, *Proceedings of the twenty-eighth annual ACM symposium on theory of computing*, 212-219, ACM,(1996).
2. P. W. Shor, Polynomial-time algorithms for prime factorization and discrete logarithms on a quantum computer, *SIAM J. Comput.* **26**(5), 1484-1509, (1997).
3. R. P. Feynman, Simulating physics with computers, *Int. J. Theor. Phys.* **21**(6), 467-488, (1982)
4. W. L. Barnes, Fluorescence near interfaces: the role of photonic mode density, *J. Mod. Opt.* **45**(4), 661-699, (1998).
5. J. L. O'Brien, A. Furusawa, and J. Vukovi, Photonic quantum technologies, *Nat. Photon.* **3**(12), 687-695, (2009).
6. J. Mower, N. C. Harris, G. R. Steinbrecher, Y. Lahini, and D. Englund, High-fidelity quantum photonics on a programmable integrated circuit, *arXiv preprint*, arXiv:1406.3255 (2014).
7. M. D. Eisaman, J. Fan, A. Migdall, and S. V Polyakov, Invited review article: Single-photon sources and detectors, *Rev. Sci. Instrum.* **82**(7), 071101, (2011).
8. M. Hijlkema, B. Weber, H. P. Specht, S. C. Webster, A. Kuhn, and G. Rempe, A single-photon server with just one atom, *Nat. Phys.* **3**(4), 253-255, (2007).
9. C. Maurer, C. Becher, C. Russo, J. Eschner, and R. Blatt, A single-photon source based on a single Ca^+ ion, *New J. Phys.* **6**, 94–94, (2004).
10. M. Steiner, A. Hartschuh, R. Korlacki, and A. J. Meixner, Highly efficient, tunable single-photon source based on single molecules, *Appl. Phys. Lett.* **90**(18), 183122, (2007).
11. A. V. Akimov, A. Mukherjee, C. L. Yu, D. E. Chang, A. S. Zibrov, P. R. Hemmer, H. Park, and M. D. Lukin, Generation of single optical plasmons in metallic nanowires coupled to quantum dots., *Nature* **450**(7168), 402–6, (2007).

12. E. Wu, J. R. Rabeau, G. Roger, F. Treussart, H. Zeng, P. Grangier, S. Prawer, and J.-F. Roch, Room temperature triggered single-photon source in the near infrared, *New J. Phys.* **9**(12), 434–434, (2007).
13. S. Chen, Y.-A. Chen, T. Strassel, Z.-S. Yuan, B. Zhao, J. Schmiedmayer, and J.-W. Pan, Deterministic and Storable Single-Photon Source Based on a Quantum Memory, *Phys. Rev. Lett.* **97**(17), 173004, (2006).
14. J. Kim, O. Benson, H. Kan, and Y. Yamamoto, A single-photon turnstile device, *Nature* **397**, 500–503, (1999).
15. A. Gruber, A. Drbenstedt, C. Tietz, L. Fleury, J. Wrachtrup, and C. Von Borczyskowski, Scanning Confocal Optical Microscopy and Magnetic Resonance on Single Defect Centers, *Science* **276**(5321), 2012–2014, (1997).
16. C. Kurtsiefer, S. Mayer, P. Zarda, and H. Weinfurter, Stable solid-state source of single photons, *Phys. Rev. Lett.* **85**(2), 290–3, (2000).
17. A. W. Schell, G. Kewes, T. Schrder, J. Wolters, T. Aichele, and O. Benson, A scanning probe-based pick-and-place procedure for assembly of integrated quantum optical hybrid devices, *Rev. Sci. Instrum.* **82**(7), 073709, (2011).
18. B. Lounis and W. Moerner, Single photons on demand from a single molecule at room temperature, *Nature* **407** (6803), 491–3, (2000).
19. X. Wang, X. Ren, K. Kahen, M. a Hahn, M. Rajeswaran, S. Maccagnano-Zacher, J. Silcox, G. E. Cragg, A. L. Efros, and T. D. Krauss, Non-blinking semiconductor nanocrystals, *Nature* **459**(7247), 686–9, (2009).
20. F. Jelezko and J. Wrachtrup, Single defect centres in diamond: A review, *Phys. Status Solidi*, **203**(13), 3207–3225, (2006).
21. T. A. Kennedy, J. S. Colton, J. E. Butler, R. C. Linares, and P. J. Doering, Long coherence times at 300 K for nitrogen-vacancy center spins in diamond grown by chemical vapor deposition, *Appl. Phys. Lett.* **83**(20),4190, (2003).
22. P. Neumann, J. Beck, M. Steiner, F. Rempp, H. Fedder, P. R. Hemmer, J. Wrachtrup, and F. Jelezko, Single-shot readout of a single nuclear spin, *Science*, **329**(5991), 542–4, (2010).
23. P. C. Maurer, G. Kucsko, C. Latta, L. Jiang, N. Y. Yao, S. D. Bennett, F. Pastawski, D. Hunger, N. Chisholm, M. Markham, D. J. Twitchen, J. I. Cirac, and M. D. Lukin, Room-temperature quantum bit memory exceeding one second, *Science*, **336**(6086), 1283–6, (2012).
24. L. Robledo, L. Childress, H. Bernien, B. Hensen, P. F. A. Alkemade, and R. Hanson, High-fidelity projective read-out of a solid-state spin quantum register, *Nature* **477**(7366), 574–8, (2011).
25. F. Dolde, I. Jakobi, B. Naydenov, N. Zhao, S. Pezzagna, C. Trautmann, J. Meijer, P. Neumann, F. Jelezko, and J. Wrachtrup, Room-temperature entanglement between single defect spins in diamond, *Nat. Phys.***9**(3), 139–143, (2013).
26. M. V. G. Dutt, L. Childress, L. Jiang, E. Togan, J. Maze, F. Jelezko, a S. Zibrov, P. R. Hemmer, and M. D. Lukin, Quantum register based on individual electronic and nuclear spin qubits in diamond, *Science* **316**(5829), 1312–6, (2007).
27. F. Dolde, H. Fedder, M. W. Doherty, T. Nbauer, F. Rempp, G. Balasubramanian, T. Wolf, F. Reinhard, L. C. L. Hollenberg, F. Jelezko, and J. Wrachtrup, Electric-field sensing using single diamond spins, *Nat. Phys.* **7**(6), 459–463, (2011).
28. J. R. Maze, P. L. Stanwix, J. S. Hodges, S. Hong, J. M. Taylor, P. Cappellaro, L. Jiang, M. V. G. Dutt, E. Togan, S. Zibrov, A. Yacoby, R. L. Walsworth, and M. D. Lukin, Nanoscale magnetic sensing with an individual electronic spin in diamond, *Nature* **455**(7213), 644–7, (2008).

29. G. Kucsko, P. C. Maurer, N. Y. Yao, M. Kubo, H. J. Noh, P. K. Lo, H. Park, and M. D. Lukin, Nanometre-scale thermometry in a living cell, *Nature* **500**(7460), 54–8, (2013).
30. A. Ajoy and P. Cappellaro, Stable three-axis nuclear-spin gyroscope in diamond, *Phys. Rev. A* **86**(6), 062104, (2012).
31. C. Santori, P. E. Barclay, K. C. Fu, R. G. Beausoleil, S. Spillane, and M. Fisch, Nanophotonics for quantum optics using nitrogen-vacancy centers in diamond, *Nanotechnology* **21**(27), 274008, (2010).
32. E. M. Purcell, Spontaneous emission probabilities at radio frequencies, *Phys. Rev.* **69**, (1946).
33. S. Schietinger and O. Benson, Coupling single NV-centres to high-Q whispering gallery modes of a preselected frequency-matched microresonator, *J. Phys. B At. Mol. Opt. Phys.* **42**(11), 114001, (2009).
34. J. Wolters, A. W. Schell, G. Kewes, N. Nsse, M. Schoengen, H. Dscher, T. Hannappel, B. Lchel, M. Barth, and O. Benson, Enhancement of the zero phonon line emission from a single nitrogen vacancy center in a nanodiamond via coupling to a photonic crystal cavity, *Appl. Phys. Lett.* **97**(14), 141108, (2010).
35. J. Riedrich-Mller, L. Kipfstuhl, C. Hepp, E. Neu, C. Pauly, F. Mcklich, A. Baur, M. Wandt, S. Wolff, M. Fischer, S. Gsell, M. Schreck, and C. Becher, One- and two-dimensional photonic crystal microcavities in single crystal diamond, *Nat. Nanotechnol.* **7**(1), 69–74, (2012).
36. A. Faraon, C. Santori, Z. Huang, V. M. Acosta, and R. G. Beausoleil, Coupling of Nitrogen-Vacancy Centers to Photonic Crystal Cavities in Monocrystalline Diamond, *Phys. Rev. Lett.* **109**(3), 033604, (2012).
37. B. J. M. Hausmann, B. J. Shields, Q. Quan, Y. Chu, N. P. de Leon, R. Evans, M. J. Burek, A. S. Zibrov, M. Markham, D. J. Twitchen, H. Park, M. D. Lukin, and M. Lonc R, Coupling of NV centers to photonic crystal nanobeams in diamond, *Nano Lett.* **13**(12), 5791–6, (2013).
38. T. Schrder, F. Gdeke, M. J. Banholzer, and O. Benson, Ultrabright and efficient single-photon generation based on nitrogen-vacancy centres in nanodiamonds on a solid immersion lens, *New J. Phys.* **13** (5), 055017, (2011).
39. J. P. Hadden, J. P. Harrison, C. Stanley-Clarke, L. Marseglia, Y.-L. D. Ho, B. R. Patton, J. L. O'Brien, and J. G. Rarity, Strongly enhanced photon collection from diamond defect centers under microfabricated integrated solid immersion lenses, *Appl. Phys. Lett.* **97**(24), 241901, (2010).
40. T. M. Babinec, B. J. M. Hausmann, M. Khan, Y. Zhang, J. R. Maze, P. R. Hemmer, and M. Loncar, A diamond nanowire single-photon source, *Nat. Nanotechnol.* **5**(3), 195–9, (2010).
41. J. T. Choy, I. Bulu, B. J. M. Hausmann, E. Janitz, I.-C. Huang, and M. Loncar, Spontaneous emission and collection efficiency enhancement of single emitters in diamond via plasmonic cavities and gratings, *Appl. Phys. Lett.* **103**(16), 161101, (2013).
42. T. Galfsky, H. N. S. Krishnamoorthy, W. D. Newman, and E. Narimanov, Directional out-coupling from active hyperbolic metamaterials,*arXiv Prepr.* arXiv1404.1535 (2014).
43. J. T. Choy, B. J. M. Hausmann, T. M. Babinec, I. Bulu, M. Khan, P. Maletinsky, A. Yacoby, and M. Lonar, Enhanced single-photon emission from a diamond–silver aperture, *Nat. Photon.* **5**(12), 738–743, (2011).
44. S. Schietinger, M. Barth, T. Aichele, and O. Benson, Plasmon-enhanced single photon emission from a nanoassembled metal-diamond hybrid structure at room temperature, *Nano Lett.* **9**(4), 1694–8, (2009).

45. A. Faraon, P. Barclay, and C. Santori, Resonant enhancement of the zero-phonon emission from a colour centre in a diamond cavity, *Nat. Photon.* **5**, 301–305, (2011).
46. D. Smith and D. Schurig, Electromagnetic Wave Propagation in Media with Indefinite Permittivity and Permeability Tensors, *Phys. Rev. Lett.* **90**(7), 077405, (2003).
47. Z. Jacob, L. V Alekseyev, and E. Narimanov, Optical Hyperlens: Far-field imaging beyond the diffraction limit, *Opt. Express* **14**(18), 8247–56, (2006).
48. A. Poddubny, I. Iorsh, P. Belov, and Y. Kivshar, Hyperbolic metamaterials, *Nat. Photon.* **7**(12), 948–957, (2013).
49. Z. Liu, H. Lee, Y. Xiong, C. Sun, and X. Zhang, Far-field optical hyperlens magnifying sub-diffraction-limited objects, *Science* **315** (5819), 1686, (2007).
50. M. A. Noginov, H. Li, Y. A. Barnakov, D. Dryden, G. Nataraj, G. Zhu, C. E. Bonner, M. Mayy, Z. Jacob, and E. E. Narimanov, Controlling spontaneous emission with metamaterials, *Opt. Lett.* **35**(11), 1863–5, (2010).
51. J.-Y. Kim, V. P. Drachev, Z. Jacob, G. V. Naik, A. Boltasseva, E. Narimanov, and V. M. Shalaev, Improving the radiative decay rate for dye molecules with hyperbolic metamaterials, *Opt. Express* **20**(7),8100–8116, (2012).
52. D. Lu, J. J. Kan, E. E. Fullerton, and Z. Liu, Enhancing spontaneous emission rates of molecules using nanopatterned multilayer hyperbolic metamaterials, *Nat. Nanotechnol.* **9**(1), 48–53, (2014).
53. Z. Jacob, J.-Y. Kim, G. V. Naik, a. Boltasseva, E. E. Narimanov, and V. M. Shalaev, Engineering photonic density of states using metamaterials, *Appl. Phys. B* **100**(1), 215–218, (2010).
54. H. N. S. Krishnamoorthy, Z. Jacob, E. Narimanov, I. Kretzschmar, and V. M. Menon, Topological transitions in metamaterials, *Science* **336**(6078), 205–9, (2012).
55. O. Kidwai, S. V. Zhukovsky, and J. E. Sipe, Effective-medium approach to planar multilayer hyperbolic metamaterials: Strengths and limitations, *Phys. Rev. A* **85**(5), 053842, (2012).
56. J. Elser, R. Wangberg, V. A. Podolskiy, and E. E. Narimanov, Nanowire metamaterials with extreme optical anisotropy, *Appl. Phys. Lett.*, **89**(26), 261102, (2006).
57. S. V. Zhukovsky, O. Kidwai, and J. E. Sipe, Physical nature of volume plasmon polaritons in hyperbolic metamaterials, *Opt. Express* **21**(12), 14982-14987, (2013).
58. M. Y. Shalaginov, V. V. Vorobyov, J. Liu, M. Ferrera, A. V. Akimov, A. Lagutchev, A. N. Smolyaninov, V. V. Klimov, J. Irudayaraj, A. V. Kildishev, A. Boltasseva, and V. M. Shalaev, Enhancement of single-photon emission from nitrogen-vacancy centers with TiN/(Al,Sc)N hyperbolic metamaterial *Laser & Photon. Rev.* **9**(1), 120–7, (2015).
59. M. A. Azzam and N. M. Bashara, *Ellipsometry and polarized light*. (North Holland, 1987).
60. M. Y. Shalaginov, S. Ishii, J. Liu, J. Irudayaraj, A. Lagutchev, A. V. Kildishev, and V. M. Shalaev, Broadband enhancement of spontaneous emission from nitrogen-vacancy centers in nanodiamonds by hyperbolic metamaterials, *Appl. Phys. Lett.* **102**(17), p. 173114, (2013).
61. G. V Naik, B. Saha, J. Liu, S. M. Saber, E. Stach, J. M. K. Irudayaraj, T. D. Sands, V. M. Shalaev, and A. Boltasseva, Epitaxial superlattices with titanium nitride as a plasmonic component for optical hyperbolic metamaterials, *Proc. Natl. Acad. Sci. U. S. A.* **111**(21), 7546-7551, (2014).
62. G. V. Naik, J. L. Schroeder, X. Ni, A. V. Kildishev, and T. D. Sands, Titanium nitride as a plasmonic material for visible and near-infrared wavelengths, *Opt. Mater.* **2**(4), 1–13, (2012).

63. U. Guler, A. Boltasseva, and V. M. Shalaev, Applied physics. Refractory plasmonics, *Science* **344**(6181), 263–4, (2014).
64. Z. Jacob, I. I. Smolyaninov, and E. E. Narimanov, Broadband Purcell effect: Radiative decay engineering with metamaterials, *Appl. Phys. Lett.* **100**(18), 181105, (2012).
65. O. Kidwai, S. V Zhukovsky, and J. E. Sipe, Dipole radiation near hyperbolic metamaterials: applicability of effective-medium approximation, *Opt. Lett.* **36**(13), 2530–2, (2011).
66. C. Bradac, T. Gaebel, N. Naidoo, J. R. Rabeau, and A. S. Barnard, Prediction and measurement of the size-dependent stability of fluorescence in diamond over the entire nanoscale, *Nano Lett.* **9**(10), 3555–64, (2009).
67. S. Mahendia, a K. Tomar, R. P. Chahal, P. Goyal, and S. Kumar, Optical and structural properties of poly(vinyl alcohol) films embedded with citrate-stabilized gold nanoparticles, *J. Phys. D. Appl. Phys.* **44**(20), 205105, (2011).
68. J. Elser, V. Podolskiy, I. Salakhutdinov, and I. Avrutsky, Nonlocal effects in effective-medium response of nanolayered metamaterials, *Appl. Phys. Lett.* **90**(19), 191109, (2007).
69. *Guide to Using WVASE 32: Spectroscopic Ellipsometry Data Acquisition and Analysis Software*, J. A. Woollam Company, Inc., (2008).
70. D. O'Connor and D. Phillips, *Time-correlated Single Photon Counting*. (Academic Press, London, 1984).
71. R. Brown and R. Twiss, Correlation between photons in two coherent beams of light, *Nature* **177**(4497), 27–29, (1956).
72. A. Beveratos, R. Brouri, T. Gacoin, J. P. Poizat, and P. Grangier, Nonclassical radiation from diamond nanocrystals, *Phys. Rev. A* **64**(6), 061802, (2001).
73. M. S. Yeung and T. K. Gustafson, Spontaneous emission near an absorbing dielectric surface, *Phys. Rev. A* **54**(6), 5227–5242, (1996).
74. J. Sipe, The dipole antenna problem in surface physics: a new approach, *Surf. Sci.* **5**, 489–504, (1981).
75. G. Ford and W. Weber, Electromagnetic interactions of molecules with metal surfaces, *Phys. Rep.* **113**(4), 195-287, (1984).
76. L. Novotny and B. Hecht, *Principles of Nano-Optics*. (Cambridge University Press, Cambridge, England 2006).
77. C. L. Cortes, W. Newman, S. Molesky, and Z. Jacob, Quantum nanophotonics using hyperbolic metamaterials, *J. Opt.* **14** (6), 063001, (2012).
78. L. F. Shampine, Vectorized adaptive quadrature in MATLAB, *J. Comput. Appl. Math.* **211**(2), 131–140, (2008).
79. M. Frimmer, A. Mohtashami, and A. F. Koenderink, Nanomechanical method to gauge emission quantum yield applied to nitrogen-vacancy centers in nanodiamond, *Appl. Phys. Lett.* **102**(12), 121105, (2013).
80. W. Chew and S. Chen, Response of a point source embedded in a layered medium, *Antennas Wirel. Propag. Lett.* **2**(1), 1–9, (2003).
81. P. Drude, Ueber Oberflachenschichten, *Ann. Phys.* **272**(4), 865-897, (1889).
82. K. Visscher, G. Brakenhoff, and T. Visser, Fluorescence saturation in confocal microscopy, *J. Microsc.* **175**(2), 162–165, (1994).
83. S. V Zhukovsky, O. Kidwai, and J. E. Sipe, Physical nature of volume plasmon polaritons in hyperbolic metamaterials, *Opt. Express* **21**(12), 14982–14987, (2013).
84. P. Yeh, Optical waves in layered media. New York: Wiley, 1988.
85. Z. Jacob, I. I. Smolyaninov, and E. E. Narimanov, Broadband Purcell effect: Radiative decay engineering with metamaterials, *Appl. Phys. Lett.* **100**(18), 181105 (2012).

86. H. J. Kimble, M. Dagenais, and L. Mandel, Photon antibunching in resonance fluorescence, *Phys. Rev. Lett.* **39**(11), 691, (1977).
87. K. Visscher, G. J. Brakenhoff, and T. D. Visser, *J. Microsc.* **175**(2), 162-165, (1994).
88. P. B. Johnson and R. W. Christy, Optical Constants of the Noble Metals, *Phys. Rev. B* **6**, 4370-4379, (1972).

Appendix: Calculation of Generalized Reflection and Transmission Coefficients of a Planar Multilayer Slab

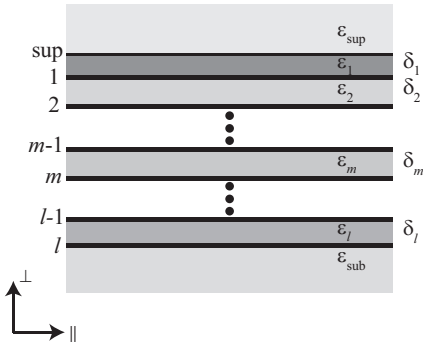

Fig. 15. Schematic of an arbitrary planar lamellar slab consisting of l layers.[58] Figure reproduced with permission from Copyright 2014 Wiley-VCH.

The generalized reflection coefficients $\tilde{r}^{(p,s)}(\omega, s)$ incorporate the reflection not only from the first interface but all the subsequent reflections from the interfaces positioned below. Therefore, $\tilde{r}^{(p,s)}$ represent the reflection from the whole multilayer structure, including the substrate. The schematic of the structure is shown in Fig. 15. Each layer is characterized by relative permittivity ε_m and thickness d_m. Above and below the multilayer slab, there are superstrate (ε_{sup}) and substrate (ε_{sub}) half-spaces.

The coefficients $\tilde{r}^{(p,s)}(\omega, s)$ are usually calculated using the transfer matrices (T-matrices). However, direct multiplication of T-matrices corresponding to the different layers result in large calculation errors and even in some cases fail to produce the output. Fig. 16 shows the relative errors when calculating the k-dependent

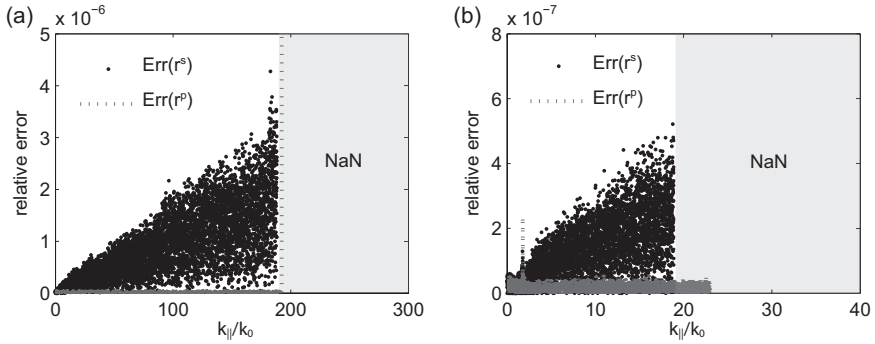

Fig. 16. Relative errors when calculating the k-dependent reflection coefficients $\tilde{r}^p$, $\tilde{r}^s$ for the binary lamellar structure made of (a) 10 and (b) 100 metal-dielectric (gold-alumina) layers.

reflection coefficients $\tilde{r}^p$, $\tilde{r}^s$ for a binary lamellar structure using direct T-matrices multiplication. The example structures in Figs. 16 (a) and (b) are made of 10 and 100 metal-dielectric pairs, respectively. The considered wavelength is 503.3 nm. The dielectric material is alumina (ε_{diel} = 3.15),[88] the metal is gold (ε_{met} = -2.69+i3.45),[88] substrate and superstrate are glass (ε_{sub} = 2.25) and air(ε_{sup} = 1), correspondingly. The thickness of each layer is 15 nm, except for the uppermost layer (alumina), which is 17-nm-thick. Above a certain value of $k_{\|}$, calculations using direct multiplication of T-matrices fail (NaN is returned). On one hand, for a fixed value of k, as the number of layers in the structure increases, the errors produced at different T-matrix multiplication steps are accumulated. On the other hand, for a fixed number of layers, larger k-vectors will negatively affect the errors during each T-matrix multiplication, because the numbers being multiplied and added become increasingly mismatched. Therefore, this calculation method restricts both the number of layers in the structure and the maximum value of the k-vector.

In order to avoid the issues of applying the direct T-matrix approach, we use the recursive invariant imbedding method.[80] In this method, in order to obtain $\tilde{r}^{(p,s)}$ instead of directly multiplying the T-matrices, the former are calculated recursively starting from the Fresnel coefficient of the last metamaterial layer. Since the recursive formula is explicit, we bypass the T-matrix multiplication and avoid the errors associated with it. As a result, our calculations converge for arbitrary numbers of layers and k-vector values.

The iterative formula to calculate $\tilde{r}^{(p,s)}(s)$ is the following

$$\tilde{r}_m^{(p,s)}(s) = \frac{r_m^{(p,s)}(s) + \tilde{r}_{m+1}^{(p,s)}(s) e^{i2k_0 s_{\perp,m}(s)\delta_m}}{1 + r_m^{(p,s)}(s)\tilde{r}_{m+1}^{(p,s)}(s) e^{i2k_0 s_{\perp,m}(s)\delta_m}}, \left(m \in \sup, \overline{1,l}\right) \tag{10}$$

where $s_{\perp,m} = k_{\perp,m}/k_0 = \left(\varepsilon_m - s^2\right)^{1/2}$, $r_m^{(p,s)}$ are the conventional single-interface Fresnel coefficients

$$r_m^p(s) = \frac{\varepsilon_m s_{\perp,m-1}(s) - \varepsilon_{m-1} s_{\perp,m}(s)}{\varepsilon_m s_{\perp,m-1}(s) + \varepsilon_{m-1} s_{\perp,m}(s)}, r_m^s(s) = \frac{s_{\perp,m-1}(s) - s_{\perp,m}(s)}{s_{\perp,m-1}(s) + s_{\perp,m}(s)}. \tag{11}$$

The iteration starts from the substrate ($\tilde{r}_{l+1}^{(p,s)}(s) = 0$), then we come up with the seeding iteration ($\tilde{r}_l^{(p,s)}(s) = r_l^{(p,s)}(s)$) and continue with the next step:

$$\tilde{r}_{l-1}^{(p,s)}(s) = \frac{r_{l-1}^{(p,s)}(s) + r_l^{(p,s)}(s) e^{i2k_0 s_{\perp,l-1}(s)\delta_{l-1}}}{1 + r_{l-1}^{(p,s)}(s) r_l^{(p,s)}(s) e^{i2k_0 s_{\perp,l-1}(s)\delta_{l-1}}} \tag{12}$$

It should be noted that (12) can be turned into the familiar Drude formula for the reflection coefficient for a single layer of thickness δ [89]:

$$r^{(p,s)}(s) = \frac{r_{1,2}^{(p,s)}(s) + r_{2,3}^{(p,s)}(s)e^{i2k_0 s_\perp(s)\delta}}{1 + r_{1,2}^{(p,s)}(s)r_{2,3}^{(p,s)}(s)e^{i2k_0 s_\perp(s)\delta}} \tag{13}$$

In the formulas (7) and 8, $\tilde{r}^p$ and $\tilde{r}^s$ are expressed as functions of a polar angle θ instead of normalized in-plane wavevector s. The relation between s and θ for the modes propagating in the superstrate medium is $s(\theta) = \varepsilon_{\text{sup}}^{1/2}\sin(\theta)$.